Classification of Sea Ice Types in ENVISAT Synthetic Aperture Radar Images

Natalia Yu. Zakhvatkina, Vitaly Yu. Alexandrov, Ola M. Johannessen, Stein Sandven, and Ivan Ye. Frolov

Abstract—In this paper, sea ice in the Central Arctic has been classified in synthetic aperture radar (SAR) images from ENVISAT using a neural network (NN)-based algorithm and a Bayesian algorithm. Since different sea ice types can have similar backscattering coefficients at C-band HH polarization, it is necessary to use textural features in addition to the backscattering coefficients. The analysis revealed that the most informative texture features for the classification of multiyear ice (MYI), deformed first-year ice (FYI) (DFYI), and level FYI (LFYI) and open water/nilas are correlation, inertia, cluster prominence, energy, homogeneity, and entropy, as well as third and fourth central statistical moments of image brightness. The optimal topology of the NN, trained for ENVISAT wide-swath SAR sea ice classification, consists of nine neurons in input layer, six neurons in hidden layer, and three neurons in output layer. The classification results for a series of 20 SAR images, acquired in the central part of the Arctic Ocean during winter months, were compared to expert analysis of the images and ice charts. The results of the NN classification show that the average correspondences with the expert analysis amount to 85%, 83%, and 80% for LFYI, DFYI, and MYI, respectively. The Bayesian pixel-based method can provide a higher resolution in the classified image and, therefore, better capability to identify leads compared to the NN method. Both methods may be effectively used in the Central Arctic where MYI is predominant.

Index Terms—Classification, neural network (NN) algorithm, sea ice, synthetic aperture radar (SAR).

N. Y. Zakhvatkina is with the Arctic and Antarctic Research Institute, Saint Petersburg, 199397, Russia, and also with the Nansen International Environmental and Remote Sensing Centre, Saint Petersburg, 199034, Russia (e-mail: natalia.piotrovskaya@niersc.spb.ru).

V. Y. Alexandrov is with the Nansen International Environmental and Remote Sensing Centre, Saint Petersburg, Russia, and also with the Nansen Environmental and Remote Sensing Center, 5006 Bergen, Norway (e-mail: vitali.alexandrov@niersc.spb.ru).

O. M. Johannessen is with the Nansen Environmental and Remote Sensing Center, 5006 Bergen, Norway, and also with the University of Bergen, Bergen, Norway (e-mail: ola.johannessen@nersc.no).

S. Sandven is with the Nansen Environmental and Remote Sensing Center, 5006 Bergen, Norway (e-mail: stein.sandven@nersc.no).

I. Y. Frolov is with the Arctic and Antarctic Research Institute, Saint Petersburg, Russia (e-mail: frolov@aari.ru).

Digital Object Identifier 10.1109/TGRS.2012.2212445

I. INTRODUCTION

SEA ice monitoring has been one of the main mission objectives for satellite programs such as RADARSAT, European Remote Sensing satellite (ERS), ENVISAT, and the upcoming Sentinel-1. With the growing amount of synthetic aperture radar (SAR) images available for sea ice observation, it is important to generate SAR data products in support of various user applications. These include sea ice research, climate studies, support to navigation in ice, and other operations in ice-covered seas. Studies of sea ice signatures in C-band SAR images over the last two decades have shown that a number of ice parameters can be determined from the images such as ice edge; ice types—multiyear, first-year, young, and new ice; fast ice boundaries; ice drift and shear zones; areas of level and deformed ice; leads; polynyas; and some other parameters [1]–[7].

Analysis of sea ice in SAR images can be done with a number of different techniques. Developing automatic ice classification methods for SAR images has been a long-standing goal for sea ice researchers and operational ice charting services [1]. SAR records the magnitude and phase of the signal backscattered from the ice surface. To form an image in the azimuth direction, these complex-valued signals are summed coherently with an appropriate phase shift [5]. The objective of sea ice classification of SAR images is to identify the main sea ice features related to ice types and surface roughness and classify them into a set of predefined categories. These categories should be in agreement with the sea ice nomenclature as defined by the World Meteorological Organization [8]. This implies that quantitative information about forms of ice, stage of development, and concentration should be derived from SAR images. This information is derived by visual inspection of SAR images in the production of operational ice charts, but this process may possibly be improved by the use of automatic algorithms.

The most straightforward method to employ SAR data for sea ice analysis is to use calibrated backscattering coefficients (σ°) for discrimination between multiyear, first-year, and some young and new ice types, but this method is hampered by ambiguities in the relation between ice types and σ° [9], [10], since different ice types can have a similar σ° [2], [11]. More advanced methods use image texture analysis, such as Markov random fields [12], [13]. An unsupervised algorithm that combines learning vector quantization and iterative maximum likelihood algorithms has been presented by Hara *et al.* [14] for the classification of polarimetric SAR images in C-, L-, and P-band data. Automated algorithms of sea ice classification and ice drift retrieval from SAR data have been implemented at the Alaska

TABLE I
LIST OF ENVISAT ASAR WS IMAGES (PIXEL SPACING OF 75 m × 75 m; 420-km SWATH WIDTH) AT HH POLARIZATION, ACQUIRED
OVER DIFFERENT ARCTIC REGIONS IN THE WINTERS OF 2005–2008 AND USED FOR ANALYSIS IN THIS STUDY

№	SAR images for angular dependencies (*) and σ° derivation		SAR images for Bayesian classification and NN training / testing		SAR images for NN classification	
	Date\ Time (UTC)	orbit	Date\ Time (UTC)	orbit	Date\ Time (UTC)	orbit
1	22 February 2005 \ 16:47	ascending	01 March 2004 \ 01:00	descending	10 March 2005 \ 16:44	ascending
2	04 March 2005 \ 16:33 *	ascending	06 December 2005 \ 16:28	ascending	15 January 2006 \ 11:27	ascending
3	05 March 2005 \ 16:01 *	ascending	15 January 2006 \ 15:32	descending	29 January 2008 \ 10:23	descending
4	10 March 2005 \ 16:44	ascending	06 March 2006 \ 15:58	ascending	31 March 2006 \ 17:52	ascending
5	27 March 2005 \ 16:10 *	ascending	31 March 2006 \ 16:14	ascending	19 April 2006 \ 16:16	descending
6	29 March 2005 \ 16:46	ascending	01 April 2006 \ 17:20	ascending	23 April 2007 \ 07:54	ascending
7	18 April 2005 \ 06:23 *	descending	18 April 2006 \ 06:58	descending	23 May 2007 \ 07:10	ascending
8	23 May 2005 \ 06:24 *	descending	07 December 2007 \ 11:54	ascending	09 December 2007 \ 12:31	ascending
9	15 January 2006 \ 15:32	ascending	09 January 2008 \ 09:38	descending	14 January 2008 \ 11:58	ascending
10	31 March 2006 \ 17:52 *	ascending	16 January 2008 \ 07:36	descending	16 January 2008 \ 10:56	ascending
11	31 March 2006 \ 16:14	ascending	06 February 2008 \ 09:56	ascending	18 January 2008 \ 09:54	ascending
12	01 April 2006 \ 15:42 *	ascending	11 December 2008 \ 01:21	ascending	19 January 2008 \ 11:01	ascending
13	01 April 2006 \ 17:20	ascending			20 January 2008 \ 10:30	ascending
14	05 April 2006 \ 16:57 *	ascending			04 February 2008 \ 10:59	ascending
15	19 April 2006 \ 16:16	ascending			05 February 2008 \ 10:28	ascending
16	07 May 2006 \ 05:12	ascending			07 February 2008 \ 09:25	ascending
17	11 May 2006 \ 16:24	ascending			08 February 2008 \ 10:33	ascending
18					15 February 2008 \ 06:53	descending
19					03 March 2008 \ 10:48	ascending
20					07 April 2008 \ 14:37	ascending

SAR Facility [15]–[17]. An approach used in the ARKTOS system includes the segmentation of SAR image, generation of descriptors for delineated segments, and use of expert system rules to classify these sea ice features [18], but this automated system needs to be further developed.

Modeling the processes and mechanisms of information processing by the human brain and their implementation in computer technologies can be used in the development of algorithms of sea ice classification from satellite images [19]–[21]. Radar image data are generally given as pixel values within a given range of digital values (usually 8 or 16 b). In order to make quantitative image interpretation, digital values of image brightness need to be recalculated to backscattering coefficients. The pulse-coupled neural network (NN) was used for ice edge detection, segmentation, and ice classification in RADARSAT SAR images of the Baltic Sea [22]. Its training was based on the assumption of Gaussian brightness distribution for different ice classes. These distributions are partially overlapped, and each pixel can belong to some ice types by detecting peaks (*modes*) in image brightness distribution. These M classes present an input of pulse-coupled NN, which determines a final value based on neighboring pixel analysis. As a result, images of new ice, level first-year ice (FYI) (LFYI), deformed FYI (DFYI), and fast ice were classified correctly, although thick fast ice was classified in some cases as thin level ice [22]. Bogdanov *et al.* [23] found that a multilayer feedforward NN, trained by a standard back-propagation algorithm, recognized six sea ice types in RADARSAT and ERS SAR images of the Kara Sea. The NN algorithm classification accuracy amounts to 71% and slightly outperforms the linear discriminant analysis algorithm, developed by Wackerman and Miller [24], whose accuracy is 68%.

The main objective of this study is to develop an NN-based sea ice classification method for SAR images, including its comparison with Bayesian approach and validation. The NN-based algorithm is developed to discriminate between LFYI, DFYI, multiyear ice (MYI), and open water/nilas (ON) in the high Arctic during winter conditions. The study includes the following steps: 1) to determine the backscattering coefficients or the normalized radar cross section from ENVISAT wide-swath (WS) SAR images (C-band HH polarization) for the four aforementioned ice types based on a selected data set from the interior of the Arctic; 2) to estimate $\sigma°$ as a function of incidence angle from the data set and normalize it to a fixed angle for each ice type; 3) to investigate and select the optimal combination of SAR image texture features for discrimination between the ice types; 4) to train the NN-based algorithm using the $\sigma°$ and the selected texture characteristics; 5) to perform classification of a test data set using the NN algorithm; and 6) to compare the NN-algorithm classification results with a Bayesian classification and to validate it by using independent data.

The results of the studies will be used to implement automatic SAR ice classification as part of the Global Monitoring for Environment and Security (GMES) services[1] for operational sea ice monitoring using data from RADARSAT-2, Sentinel-1, and other SAR satellites.

II. SELECTION AND PREPROCESSING OF SAR DATA

A. Backscattering Coefficients for Different Ice Types

A series of 14 ENVISAT Advanced Synthetic Aperture Radar (ASAR) WS images (pixel spacing of 75 m × 75 m; 420-km swath width) at HH polarization, acquired over different Arctic regions in the winters of 2005 and 2006, were used
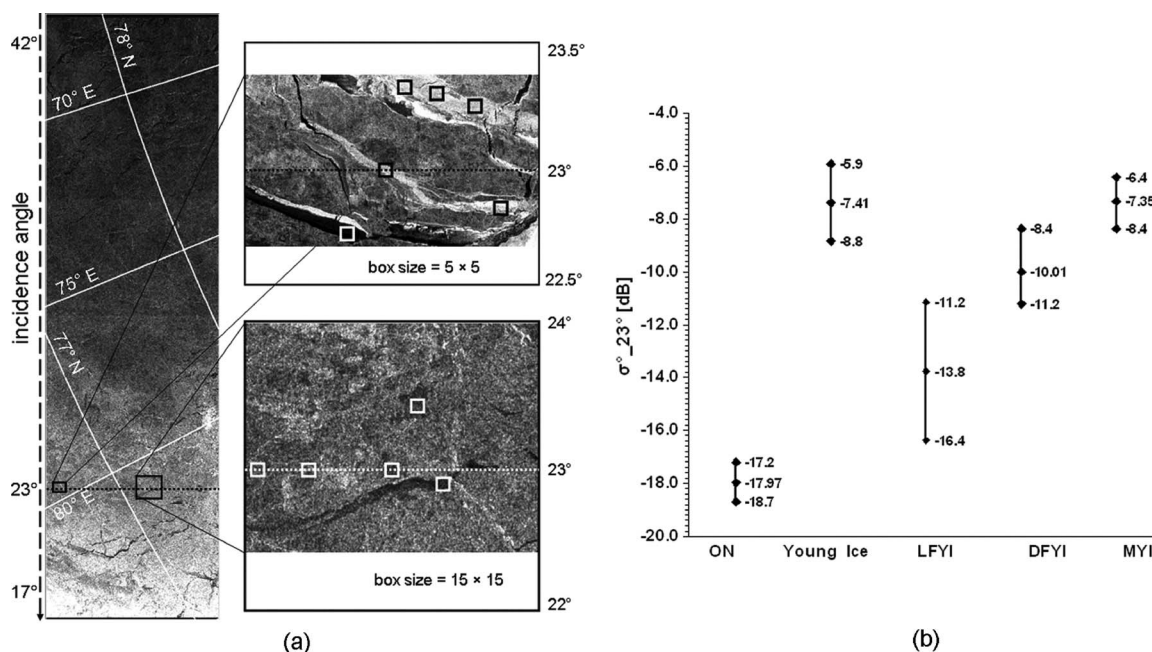
---

[1]http://www.gmes.info/

Fig. 1. (a) Fragment of original ENVISAT WS SAR image (HH polarization), taken over the northern part of the Kara Sea on April 18, 2005, at 06:22 UTC. (Right) Extracted fragments show examples of squares (5×5 and 15×15 pixels) selected in a SAR image for the estimation of σ° for different ice types at a 23° incidence angle. (b) Estimated σ° values for various ice types derived from calibrated ENVISAT WS SAR images (HH polarization) at a 23° incidence angle.

for the analysis of the sea ice backscatter (Table I). Calibration of the backscatter values to σ^0 was done using

$$\sigma^0 = \frac{A^2}{K} \sin(\alpha_D) \qquad (1)$$

where K is the absolute calibration constant, A^2 is the average pixel brightness, and α_D is the incidence angle for each pixel [25]. The major factor, limiting measurement accuracy for calibrated radar, is a number of noncoherent sums, i.e., speckle noise [26].

The backscatter coefficients for five sea ice types (ON, young ice, LFYI, DFYI, and MYI) were derived for an incidence angle of 23°. This angle was selected for comparison with literature data on sea ice backscatter at VV polarization, mostly derived from ERS SAR images. The defined ice types were delineated in the 14 ENVISAT ASAR images based on an expertise in image interpretation, obtained in a number of subsatellite experiments in the Arctic [5], as well as using visual sea ice observations and *in situ* measurements, conducted during the expedition on board *research vessel Mikhail Somov* in April–May 2006 in the northeastern part of the Barents Sea. We used only those parts of the ASAR images where the incidence angle is $23^\circ \pm 0.5^\circ$ as is shown in Fig. 1(a). The backscatter coefficients were averaged in squares of size 5×5 or 15×15 pixels [Fig. 1(a)]. We selected areas of 5×5 for young ice, because this ice type was observed in limited parts of the images (leads). The typical size of FYI and MYI floes was larger, and we used areas of 15×15 pixels. The mean and ranges of σ° for the five ice types were calculated from a total of 29 (ON), 22 (young ice), 1050 (LFYI), 200 (DFYI), and 450 (MYI) squares, respectively; these are summarized in Fig. 1(b).

Open water in the case of low wind speed and dark nilas have low σ° in C-band due to the near-specular reflection of electromagnetic waves from their level surfaces [27], [28]. Beaven *et al.* [29] showed that σ° for dark nilas at a 35° incident angle was about -24 dB and, for light nilas, between -19 and -20 dB. Dark nilas mostly has a bare surface, and light nilas can be covered with frost flowers. According to [30], the frost-flower-covered light nilas has approximately 6 dB higher backscatter than the bare light nilas for all incidence angles. Our analysis of ENVISAT WS SAR data, described in [31] and [32], shows σ° between -18.7 and -17.2 dB for nilas [Fig. 1(b)], which is slightly higher than values -22 and -24 dB at VV polarization, reported by Askne *et al.* [27] and Kwok *et al.* [28]. The term nilas is used here, because it is difficult to distinguish dark nilas and light nilas, when visual observations are unavailable.

Young ice is subdivided into gray and gray-white ice types [8]. For young ice, the σ° was between -8.8 and -5.9 dB [Fig. 1(b)], which is approximately 10 dB more than that for nilas. This result is in agreement with Melling [33], who reported a 10–15-dB increase of σ° for young ice when it is completely covered with frost flowers. In most cases, this difference is explained by the presence of frost flowers but can also come from snow [30]. In some cases, the high backscatter of young ice can be caused by its rafted/ridged-to-100% surface.

For LFYI, backscatter coefficients vary from -16.4 to -11.2 dB for drifting ice and from -17.5 to -15.0 dB for fast ice. DFYI has a much higher σ°, varying from -11.2 to -8.4 dB. For MYI, σ° values are even higher, with values from -8.4 to -6.4 dB [Fig. 1(b)]. These ice types can be roughly separated by a threshold of -12 dB in HH polarization [6]. The backscatter coefficients for some sea ice types have significant overlap [11], [34]. Young ice overlaps with the σ°
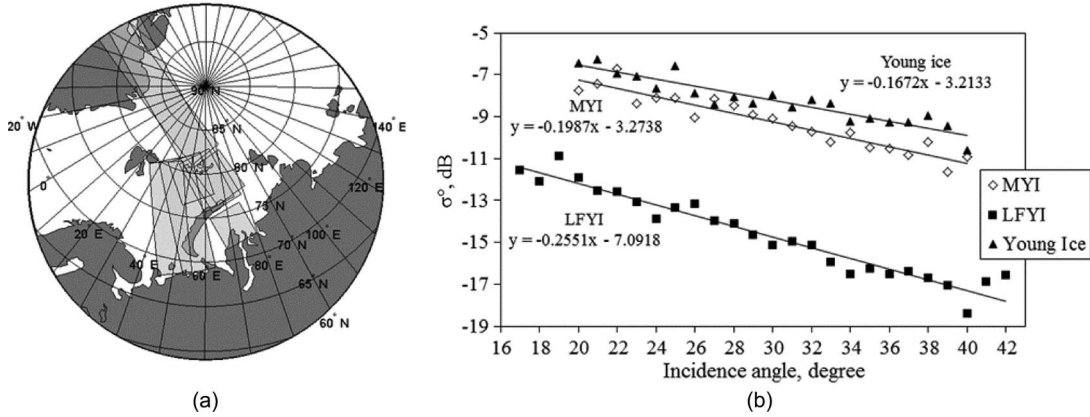
Fig. 2.   (a) Location of ENVISAT WS SAR images used in the analysis of σ° for the selected ice types. (b) σ° as a function of incidence angle for various ice types calculated from ENVISAT WS SAR images (HH polarization). Young ice—three profiles with 78 squares, LFYI—five profiles with 130 squares, and MYI—five profiles with 130 squares. The dots are estimated from observations, while the straight line is a linear fit to the data.

of DFYI and MYI. Young ice and MYI have a near-similar backscatter [Fig. 1(b)]. LFYI has a wide range of backscatter and partly overlaps with DFYI and very little with ON. ON has a low backscatter, which is different from that for other ice types. Therefore, our analysis confirms with earlier studies that additional image features need to be used in automatic sea ice classification in SAR images.

B. Backscattering Coefficients as a Function of Incidence Angle

The angular dependences of the sea ice backscatter have been derived from the eight ENVISAT ASAR WS calibrated images at HH polarization given in Fig. 2(a) and Table I. The backscattering coefficients were determined for incidence angle steps of 1° for the selected squares in the SAR images for young ice, LFYI, and MYI [Fig. 2(b)]. These ice types were observed continuously across the ENVISAT ASAR swath for the incidence angle range of 17°–42°. The DFYI and ON samples occupied only limited parts of the swath, which precluded obtaining their backscatter angular dependences. The decrease in σ° as a function of incidence angle for the various sea ice types is shown in Fig. 2(b). These data show that the decrease in σ° with increasing incidence angle is larger in absolute value for LFYI (-0.255 dB/$^\circ$) than for MYI (-0.196 dB/$^\circ$) and for young ice (-0.167 dB/$^\circ$). The decrease of σ° for LFYI with incidence angle falls into the range given by [35] (from -0.15 to -0.37 dB/$^\circ$). The change of MYI backscatter with incidence angle significantly exceeds in absolute value those for VV polarization from -0.03 to -0.1 dB/$^\circ$, presented in [35], and -0.08 dB/$^\circ$ in [36]. Our estimates for young ice are not significantly different from the value of -0.17 dB/$^\circ$ for thin FYI used in [36].

In order to classify SAR images where σ° is a function of incidence angle, the σ° values are normalized across the swath, using 25° as a reference angle and a linear function for predominant ice type as shown in Fig. 2(b). Although the difference in radar backscatter between different ice types is slightly higher at far range of SAR image, we used 25° angle, which allows analyzing SAR image without brightness amplification and also following the recommendation by R. Kwok. The predominant

ice type is identified by means of SAR image visual inspection. The normalization method consists of the following stages: 1) recalculation of image brightness to the backscatter coefficient according to (1); 2) backscatter recalculation to 25° incidence angle using the calculated coefficients [Fig. 2(b)]; and 3) recalculation of the derived backscatter coefficient to corrected brightness [29]. The backscatter normalization to predefined incidence angle allows obtaining a homogenous image contrast across the swath. The incidence angle of 25° provides a satisfactory contrast between various ice types. With the difference between the σ° angular dependences for MYI and FYI of 0.05 dB/$^\circ$, an error of using a function for MYI over a predominantly FYI area in the far range of SAR image (42°) amounts to 0.75 dB, which is within the range of its σ° standard deviation.

III. METHODS USED IN SAR IMAGE CLASSIFICATION

A. Bayesian Classification Method

In this paper, a Bayesian algorithm is implemented for sea ice classification in the SAR images. This method accounts for differences in the probability density functions and allows minimizing the error rate, if, for example, FYI has a larger variance of σ° compared to MYI [16]. We also believe that a Bayesian algorithm is suitable for the Central Arctic, where MYI dominates, so its *a priori* probability is quite high. For using this technique, the distribution densities and *a priori* probabilities of the ice types have to be estimated.

The elaborated algorithm is pixel-based and uses *a priori* probability of occurrence of given ice types. *A posteriori* probability $p(\omega_j/x_i)$ for various sea ice classes is calculated as [37]

$$p(\omega_j/x_i) = p(x_i/\omega_j) \times p(\omega_j)/p(x_i),$$

$$p(x_i) = \sum_{j=1}^{N} p(x_i/\omega_j) \times p(\omega_j). \qquad (2)$$

Here, $p(\omega_j)$ is the *a priori* probability and $p(x_i/\omega_j)$ is the conditional probability of x_i for ω_j class.
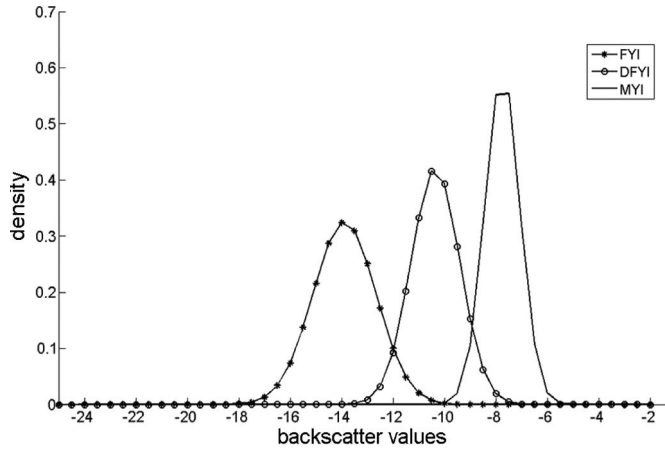
Fig. 3. Probability density functions of $\sigma°$, derived from calibrated ENVISAT ASAR images in the Central Arctic for incidence angles of 25° for MYI, LFYI, and DFYI.

Fig. 4. NN topology.

Conditional probabilities $p(x_i/\omega_j)$ were assessed from calibrated ENVISAT WS SAR images, where areas typical for each ice type were delineated visually and histograms of the backscattering coefficients were calculated (Fig. 3). Statistically significant estimates of conditional probabilities were derived for MYI, DFYI, and LFYI. MYI dominates in the Central Arctic, where its partial concentration amounts to 90%. The partial concentration of other ice types (LFYI, DFYI, young ice, and nilas) does not exceed 10% [5]. Due to the absence of reliable estimates of conditional probabilities for ON and young ice, we made an assumption that three ice types (MYI, LFYI, and DFYI) are observed in the Central Arctic and their *a priori* probabilities are 0.9, 0.05, and 0.05, respectively. Here, we also assume that leads in the MYI are covered with LFYI. Classification was made for these three ice classes.

Decision is made in favor of

ω_{my}, if $p(\omega_{my}/x_i) > p(\omega_{fy}/x_i)$ and $p(\omega_{my}/x_i) > p(\omega_{fd}/x_i)$

ω_{fy}, if $p(\omega_{fy}/x_i) > p(\omega_{my}/x_i)$ and $p(\omega_{fy}/x_i) > p(\omega_{fd}/x_i)$

ω_{fd}, if $p(\omega_{fd}/x_i) > p(\omega_{my}/x_i)$ and $p(\omega_{fd}/x_i) > p(\omega_{fy}/x_i)$.

The probability error is given by the equation

$$p(e) = \sum_{i=1}^{N}(1 - p(\omega_j/x_i)) \times p(x_i)$$
$$= \sum_{i=1}^{N} p(x_i) - p\,(x_i/\omega_j) \times p(\omega_j)). \qquad (3)$$

In this paper, Bayesian classification was mostly used for comparison with NN classification. Several of the SAR images of the Central Arctic, shown in Fig. 2(a), were classified using this approach.

B. NN Classification Method

NN models have received much attention during recent decades for the classification of satellite images. An NN may have one or more hidden layers of neurons between the input and output layers (Fig. 4). They have a simple layer structure in which successive layers of neurons are fully interconnected,
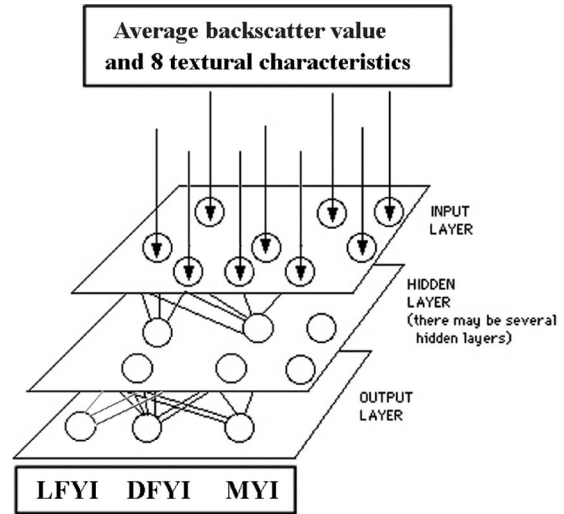
with connection weights controlling the strength of the connections. The input to each neuron in the next layer is the sum of all its incoming connection weights multiplied by their connecting input neural activation value (activation function). Empirical comparisons showed that an NN could outperform standard parametric statistical classifiers as long as a sufficient number of representative training samples are presented to its input [38]. Moreover, an NN can be used for data fusion without the determination of their informational content and any prior assumptions on the statistical distribution of the data [38], [39].

We use supervised training, which requires a teacher. In supervised training, both the inputs and the outputs are provided. In our case, the training phase of the NN was based on the back-propagation learning rule to minimize the mean square error (mse) between the desired target vectors and the actual output vectors. Training patterns were sequentially presented to the network, and the weights of each neuron were adjusted so that the approximation created by the NN minimized the global error between the desired output and the summed output created by the network. During the training of an NN, the same set of data is processed many times as the connection weights are refined [39]. The data set was split into two parts for training process: 1) data set for NN training and 2) validation data set, used to determine the performance of an NN on independent patterns. MSE has to decrease during training. The training stopped in the following cases: 1) insignificant decrease of mse during a long time (several hours or one day—depending on NN topology) and 2) curves of training and validation data sets starting to diverge.

IV. CLASSIFICATION OF SEA ICE TYPES IN SAR IMAGES USING TEXTURE FEATURES

A. Analysis of SAR Image Texture Features

The NN algorithm uses both backscatter data and textural characteristics of the images. Several studies have shown that SAR sea ice classification accuracy is improved by using image texture features [23], [40]. Texture depends on the spatial scale of sea ice surface and volume inhomogeneity, as well

as on radar spatial resolution. Texture features describe spatial variations of image brightness within a group of neighbor pixels large enough to calculate statistically significant estimates. A given texture feature can be different from one ice type to another and reflect variability in sea ice properties sensed by the SAR.

Before texture can be used in classification, it is necessary to investigate which texture features are useful for differentiation between the ice types defined in this study. A set of texture features has therefore been calculated in a number of SAR images using gray-level co-occurrence matrix (GLCM), which is determined as

$$S_{d,\alpha}(i,j) = \frac{P_{d,\alpha}(i,j)}{\sum_{i=1}^{K}\sum_{j=1}^{K} P_{d,\alpha}(i,j)} \tag{4}$$

where $S_{d,\alpha}$ is an element of GLCM, $P_{d,\alpha}$ is the number of neighbor pixel pairs, α is fixed vector directions or orientation $(0°, 45°, 90°,$ or $135°)$, d is the co-occurrence distance (between pixels), and K is the number of quantized gray levels in the image [41]. $S_{d,\alpha}$ is computed along directions α using different displacement values, also called "interpixel distance" $d = 1, \ldots, K-1$, where $i, j = 0, \ldots, K-1$. Each element (i,j) of the matrix represents the probability that two pixels, located at an "interpixel distance" d, have brightnesses i and j.

The number of brightness levels which is optimal for calculating texture parameters is typically 16 according to [23], [40], and [42]. To improve ice classification accuracy, Clausi [43] has shown that GLCM should be averaged for four different directions to account for possible rotation of the ice. The size of GLCM square is equal to the number of image brightness bins K [41], [44]. A number of texture features, such as correlation, inertia, homogeneity, and others, can be calculated from GLCM [41], [45], [46]. After $\sigma°$ normalization to a $25°$ incidence angle, nine texture features—correlation, inertia, cluster prominence, energy, homogeneity, and entropy, as well as third and fourth central statistical moments of image brightness—have been calculated in this study. This has been done for a set of images representing relatively homogeneous areas of each of the four ice types in this study (LFYI, DFYI, MYI, and ON). Ice type ON represents a mixture of new ice (grease ice), nilas, and calm open water, which all have a low backscatter and therefore cannot be further discriminated without additional data. The selected images do not contain homogeneous ice types because some mixing of ice forms and degree of deformation usually occur in sea ice areas. The normalized texture value for each texture feature and ice type has been calculated for four window sizes (16, 32, 64, and 128 pixels), and the results are shown in Fig. 5. Classification accuracy is improved when the separation of the normalized texture values for the ice types increases. Visual examination of mean texture values (Fig. 5) suggested that the 32×32 sliding window provides better separation of the ice types compared to other window sizes.

A change of distance d between neighboring pixels in (4) is also important in the calculation of GLCM [42], [44]. The same data set as used in Fig. 5 was used to analyze variation in the texture parameters for values of d of 2, 4, 8, and 16 pixels,
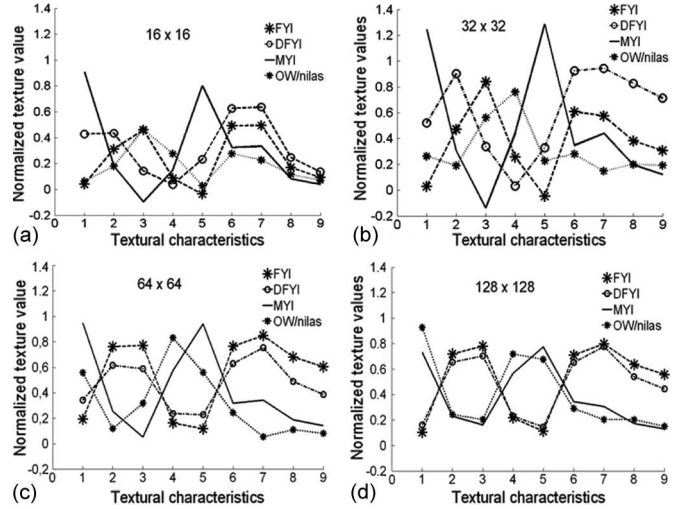

Fig. 5. Normalized mean values of texture characteristics for LFYI, DFYI, MYI, and ON, calculated for different window sizes: (a) 16×16 pixels, (b) 32×32 pixels, (c) 64×64 pixels, and (d) 128×128 pixels. [(1) Average sea ice backscatter, (2) energy, (3) correlation, (4) inertia or contrast, (5) cluster prominence, (6) homogeneity, (7) entropy, (8) third central statistical moment of brightness, and (9) fourth central statistical moment of brightness.] The calculations were made for the images shown in Fig. 2(a).
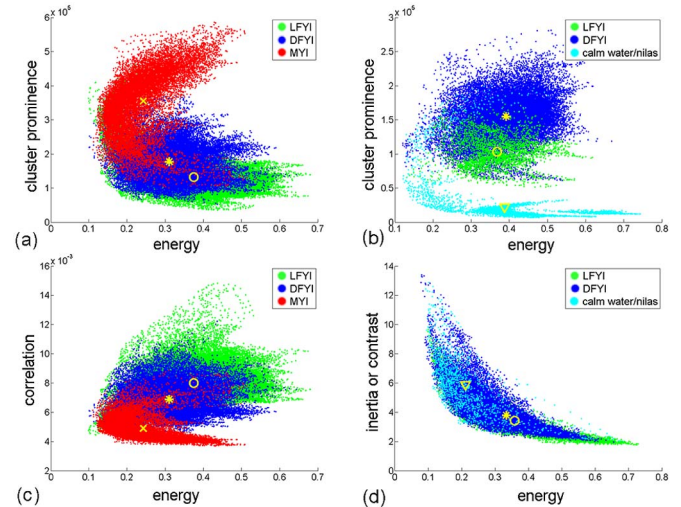

Fig. 6. Four examples of scatter plots showing how two textural features calculated from subimages in ENVISAT WS data can be used to classify ice types (LFYI, ON, DFYI, and MYI). ENVISAT WS ASAR image (HH polarization) for the following: April 23, 2007, at 07:54 UTC, the Central Arctic; April 18, 2005, at 06:22 UTC, the northern part of the Kara Sea; and January 18, 2008, at 09:55 UTC, the northern part of the Kara Sea. (Round) Center of LFYI, (asterisk) center of DFYI, (cross) center of MYI, and (triangle) center of ON.

using a window size of 32×32 pixels. Calculations were done for all textural features, and visual comparison showed that the best discrimination between the ice types was obtained for $d = 4$.

Presentation of scatterplots of the values of two texture features is a convenient way to illustrate which features are more useful for discrimination between the sea ice types. It was found that the cluster prominence versus energy and correlation versus energy provide good separation between LFYI, DFYI, and MYI [Fig. 6(a) and (c)]. Separation of ON can be done by the use of cluster prominence versus energy and, to some degree, by inertia/contrast versus energy [Fig. 6(b) and (d)]. An example of

TABLE II
CORRELATION MATRIX, CALCULATED FROM SAR IMAGES FOR FOUR ICE TYPES

Level first-year ice

	EN	COR	IN	CP	HOM	ENT	3CM	4CM
COR	0.68	1						
IN	-0.89	-0.72	1					
CLpr	-0.71	-0.95	0.75	1				
HOM	0.95	0.7	-1	-0.73	1			
ENT	0.97	0.73	-1	-0.76	0.96	1		
3CM	0.97	0.57	-0.8	-0.59	0.89	0.9	1	
4CM	0.89	0.43	-0.7	-0.46	0.8	0.78	0.97	1
AB	-0.68	-0.99	0.72	0.98	-0.71	-0.74	-0.6	-0.4

Deformed first-year ice

	EN	COR	IN	CP	HOM	ENT	3CM	4CM
COR	-0.35	1						
IN	-0.91	0.33	1					
CLpr	0.34	-0.97	-0.3	1				
HOM	0.93	-0.35	-1	0.34	1			
ENT	0.98	-0.34	-0.9	0.32	0.93	1		
3CM	0.99	-0.34	-0.9	0.34	0.91	0.9	1	
4CM	0.94	-0.31	-0.8	0.31	0.86	0.9	0.98	1
AB	0.38	-0.99	-0.4	0.99	0.38	0.4	0.37	0.33

Multiyear ice

	EN	COR	IN	CP	HOM	ENT	3CM	4CM
COR	0.33	1						
IN	-0.87	-0.3	1					
CLpr	-0.3	-0.97	0.28	1				
HOM	0.93	0.39	-1	-0.36	1			
ENT	0.97	0.27	-0.9	-0.25	0.93	1		
3CM	0.97	0.39	-0.8	-0.35	0.87	0.9	1	
4CM	0.88	0.41	-0.7	-0.37	0.78	0.78	0.97	1
AB	-0.27	-0.99	0.25	0.99	-0.34	-0.21	-0.3	-0.4

Calm open water

	EN	COR	IN	CP	HOM	ENT	3CM	4CM
COR	0.27	1						
IN	-0.9	-0.34	1					
CLpr	-0.47	-0.89	0.5	1				
HOM	0.97	0.32	-1	-0.5	1			
ENT	0.98	0.32	-1	-0.5	0.98	1		
3CM	0.95	0.14	-0.8	-0.3	0.88	0.9	1	
4CM	0.82	0.01	-0.6	-0.2	0.73	0.7	0.96	1
AB	-0.2	-0.98	0.3	0.92	-0.3	-0.3	-0.1	0.04

EN = Energy, COR = correlation, IN = inertia, CP = Cluster prominence, HOM = Homogeneity, ENT = Entropy, 3CM = 3rd central moment, 4CM = 4th central moment, AB = Average backscatter.

poor separation between two classes is shown in Fig. 6(d) where LFYI and DFYI have overlapping values of inertia/contrast versus energy. The correlation coefficients between all pairs of texture features for each of the four ice types are calculated and presented in the correlation matrices in Table II. When there is high correlation between two textural characteristics, they show the similar properties of the ice type, and it makes no sense of using both features. In case of low correlation, both features will contribute to the improvement of the sea ice classification accuracy [43]. In Table II, all correlations with an absolute value less than 0.7 are marked in gray, highlighting which pairs of texture features are useful for classification. The correlation matrices can thus be used to divide the correlation pairs into two groups: Group 1 is defined by high internal correlation and consists of energy, inertia, homogeneity, entropy, and third and fourth statistical moments. Group 2 includes correlation and cluster prominence and is characterized by moderate and low correlation with group 1 but high correlation internally. In group 2, backscatter is also included.

It is known from previous studies [44], [45] that energy, inertia, and homogeneity characterize the repeatability and spatial distribution of neighboring pixels. Therefore, inertia and homogeneity are well correlated with each other but with a negative sign. MYI and ON can be better discriminated by combinations of earlier defined features, namely, energy, inertia, homogeneity, entropy, and central statistical moments together with the correlation, cluster prominence, and mean backscatter, which are characterized by moderate and low correlation coefficients. A similar combination of texture features but with a negative sign of correlation coefficients was found for DFYI. Correlation, cluster prominence, and backscatter coefficient in combination with the third and fourth statistical moments of brightness, as well as joint use of correlation and energy, inertia, and fourth statistical moment of brightness are most important for the discrimination of LFYI.

Statistical analysis showed that the entire set of selected texture features can be used for the discrimination of the four ice types. Therefore, all eight texture features and the backscatter coefficients, shown in Table II, have been used as input for the creation, training, and determination of the NN parameters.

B. NN Classification Technique

Based on texture features analyzed in the previous section, the NN was trained for sea ice classification for the high Arctic during winter conditions. The training consisted of the following steps: 1) analysis of 12 SAR images (Table I) by three experienced ice scientists for the delineation of the polygons of the ice types to be classified; 2) preliminary image processing (see Section II) and calculation of texture features using sliding window and interpixel distance described in Section IV-A; and 3) selection of the NN topology (Fig. 4) and training data set.

Step 1 consisted of the following: Twelve SAR images of various sea ice types were selected and prepared for NN training in the Central Arctic during winter conditions (Fig. 7, marked by the light tone, and Table I). Ice experts at the Arctic and Antarctic Research Institute (AARI) delineated a number of homogenous areas for each ice type in the images. The 12 SAR images were divided into two groups: one for training and one for testing as described in step 3.

In step 2, the homogenous areas defined by AARI experts were used to calculate texture characteristics and backscattering coefficient values for each ice type. A database was established where the texture characteristics for all homogenous areas of the four ice types were included.

Step 3 consisted of a cyclic process where, first, an NN topology was selected based on the initial and, later, analyzed data [39] as described in Section III-B. The database of textural characteristics and backscatter values was used for NN training as preparation for sea ice classification of new
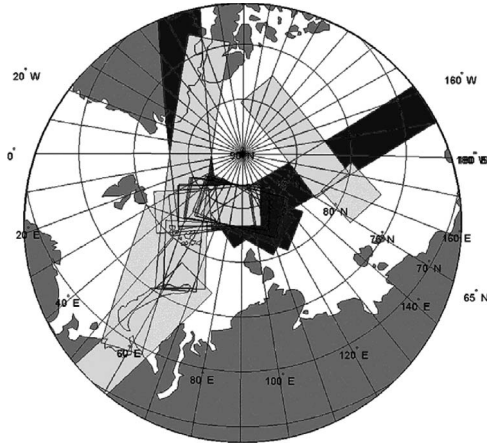
Fig. 7. Location of ENVISAT ASAR images, used for NN training (12 image stripes in light tone) and classification (20 images—dark tone). Several images were divided in two parts, one for training and one for classification.

SAR images, listed in Table I. The Stuttgart Neural Network Simulator software was used to implement the NN classification method (ftp.informatik.uni-tuebingen.de). The trained NN was then used to classify a set of test images (Table I). The classification results were visually compared by the sea ice expert's classification [similar to Figs. 3(b) and 9(b)]. Step 3 was then repeated using different NN topologies with various numbers of hidden layers and neurons in these layers until the optimal NN architecture was found based on the comparison with ice expert classification. More than 50 NNs were trained, each with nine input neurons and three or four output neurons, corresponding to the number of sea ice classes. These NNs had different numbers of hidden layers (1, 2, or 3) and neurons in these layers. The numbers of neurons in hidden layers varied from 6 to 50. MSE varied from 0.5 to 0.015.

The optimal NN topology for ENVISAT ASAR sea ice image classification was selected based on the analysis of ice expert's classified input data as well as on processing time. The selected topology consisted of nine neurons in input layer, which correspond to the number of used features, six neurons in hidden layer, and three neurons in output layer (Fig. 4). The output neurons correspond to classes of LFYI, DFYI, and MYI. MSE amounted to 0.015 in this case. The trained NN was applied to the training data set to check if the ice classes initially defined in the training data set could be reproduced. The outputs for each pattern were calculated and compared with the actual outputs from the training data set. Correspondences were 96.7% for MYI, 98% for DFYI, and 97% for LFYI. This test suggested that the NN classification algorithm is self-consistent. Another NN was trained to classify ON, LFYI, DFYI, and MYI types using ON areas, delineated in the same SAR images in addition to the previously determined data sets of LFYI, DFYI, and MYI (see step 1). The optimal topology of this NN consists of 9, 15, and 4 neurons in input, hidden, and output layers, respectively.

The trained NN was then applied for the automated classification of 20 new SAR images, listed in Table I. Each SAR image was first preprocessed with the angular correction for the predominant ice type for an incidence angle of 25° as described in Section II, followed by calculation of texture characteristics for the whole image.

TABLE III
MAIN DIAGONAL OF THE CONFUSION MATRICES FOR COMPARISON OF CLASSIFICATION RESULTS, APPLIED TO ENVISAT ASAR IMAGES, USED FOR NN TRAINING/TESTING AND BAYESIAN APPROACH, WITH AARI ICE CHARTS

SAR images, used for Bayesian classification and NN training / testing	Accuracy (NN with AARI ice chart zones – MYI and FYI),%		Accuracy (Bayes with AARI ice chart zones – MYI and FYI), %	
Date\ Time (UTC)	MYI	LFYI+ DFYI	MYI	LFYI+ DFYI
01 March 2004 \ 01:00	no AARI ice chart			
06 December 2005 \ 16:28	85.8	95.2	79.0	98.2
15 January 2006 \ 15:32	82.3	83.1	87.0	97.1
06 March 2006 \ 15:58	no AARI ice chart			
31 March 2006 \ 16:14	85.3	97.0	40.1	96.2
01 April 2006 \ 17:20	91.0	91.0	68.2	98.7
18 April 2006 \ 06:58	68.2	87.4	63.3	93.5
07 December 2007 \ 11:54	87.6	93.4	89.8	99.4
09 January 2008 \ 09:38	64.5	89.6	61.3	88.2
16 January 2008 \ 07:36	76.6	95.2	51.0	95.3
06 February 2008 \ 09:56	63.36	99.9	79.5	91.6
11 December 2008 \ 01:21	89.3	90.5	61.1	89.7
Total accuracy	**79.3**	**92.2**	**68.1**	**95.6**

V. RESULTS

A. Results from the NN Algorithm

NN quality was assessed by means of sea ice classification in the SAR images used for training (Table I). The results of classification were compared with AARI ice charts (www.aari.ru), which depict the distribution of open water and sea ice types—nilas, young, first-year, and old ice during the winter period (1.XI-31.V). Ice charts are issued every Thursday using data collected and averaged for the preceding two to five days. These charts are based on the generalization of regional ice charts, compiled from visible, infrared (IR), and radar satellite images and reports from coastal stations and ships. Confusion matrices, describing how well an algorithm can classify data, were calculated to get a quantitative measure of the classification method accuracy. The total correspondences of NN classification results and ice charts (diagonal elements of confusion matrix) were 79.3% for MYI and 92.2% for FYI (Table III).

Classification with the NN algorithm was then carried out for LFYI, DFYI, and MYI and, in the case of the second NN also, for ON for a total of 20 ASAR images in the Central Arctic (Fig. 7). The classification results were compared with ice analysis of the same SAR images performed by ice experts at AARI. The ice experts estimated visually the partial concentration for each ice type corresponding to the NN classes. This partial concentration was then compared with the partial percentage of each ice class from the NN analysis. The percentage of correspondence between the NN classification and expert analysis for the whole classified image was given in the confusion matrix. The classification results were also validated by field observations near the "North Pole-35 (NP-35)" drifting station. Airplane observations and *in situ* measurements showed that the ice floe where the "NP-35" station was located was a mixture of MYI floes of various size, thickness, and configuration. In many cases, MYI floes are separated by stripes of FYI with inclusions
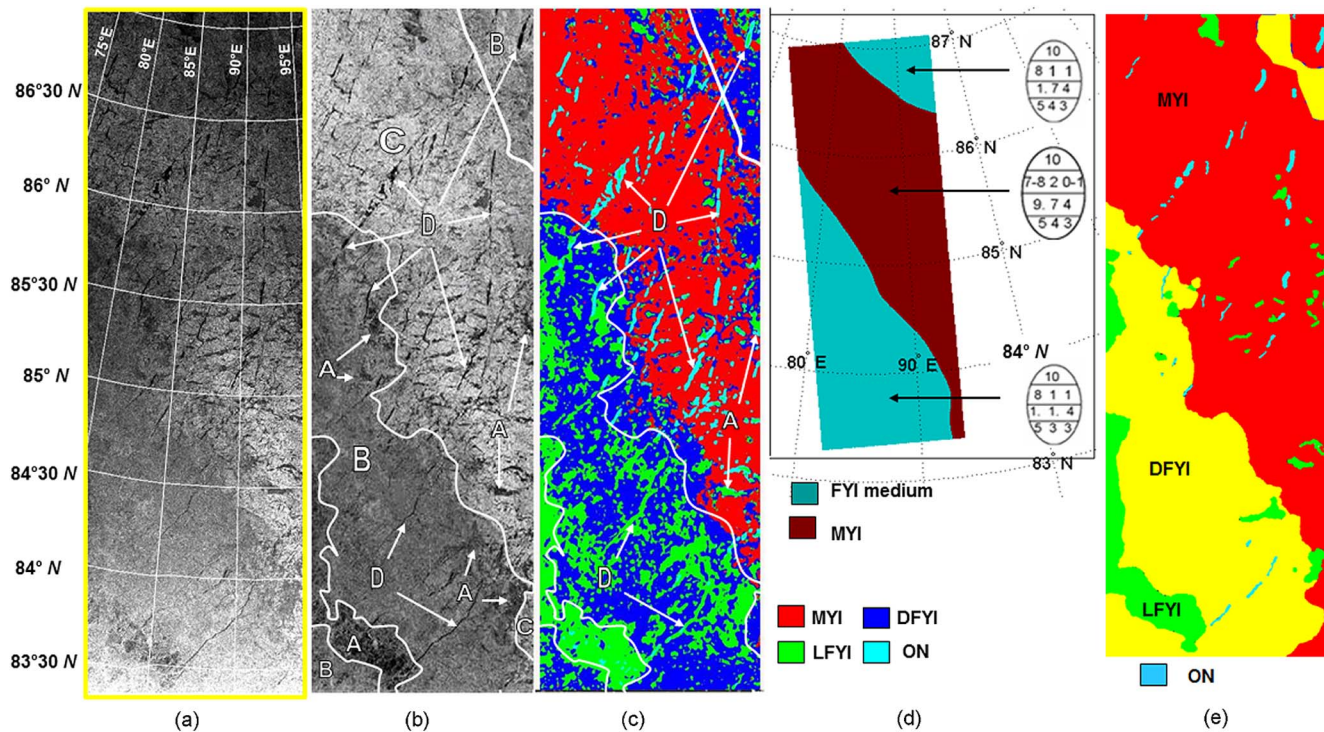
Fig. 8. (a) Fragment of original ENVISAT WS SAR image (HH polarization), taken over north of the Kara Sea on January 18, 2008, at 09:55 UTC. (b) Fragment of SAR image with normalized $\sigma°$ to an incidence angle of $25°$ and analysis by an ice expert from AARI: A is LFYI, where ridges cover less then 20% of the ice surface; B is FYI, where ridges cover more than 40% of the ice surface; C is MYI area; and D is ON. Arrows show the location of small ice features, marked by corresponding characters. (c) Result of the NN classification of four ice types where the class ON is included. (d) Ice chart provided by AARI for January 16–18, 2008. The lower legend is for the SAR classification, and the upper legend is for the ice chart. (e) Manually colored image according to sea ice expert's visual analysis.

TABLE IV

CONFUSION MATRICES FOR COMPARISON OF NN AND BAYESIAN CLASSIFICATION RESULTS, APPLIED TO ENVISAT ASAR IMAGES, WITH VISUAL EXPERT ESTIMATION. (A) JANUARY 18, 2008, [FIG. 8(C)] AND (B) FEBRUARY 4, 2008 [FIG. 9(C)]

		January 18, 2008						February 04, 2008		
		Visual expert analysis zone * :						Visual expert analysis zone ** :		
		C	A	B	D			C	A	B+D
NN class. result	MYI	64.76	6.49	25.37	3.39	NN class. result	MYI	72.15	2.46	25.35
	LFYI	0.87	86.18	10.95	1.99		LFYI	0.71	62.08	37.19
	DFYI	1.26	23.58	73.49	1.67		DFYI	15.61	11.06	73.29
	ON	12.98	34.77	14.06	38.19					
Bayes class. result	MYI	52.38	8.27	39.36	7.23	Bayes class. result	MYI	67.96	2.46	29.59
	LFYI	0.51	94.36	5.13	70.9		LFYI	0.47	73.14	26.39
	DFYI	0.82	74.29	24.89	21.86		DFYI	14.17	29.93	55.90

* SAR image was divided into zones of 4 ice types visually by sea ice experts (Fig. 8 b): A is LFYI, where ridges cover less then 20% of ice surface, B is first-year ice, where ridges cover more than 20% of ice surface, C is MYI area, and D is ON. The ice types inside each zone were missed.

** SAR image was divided into zones of 3 ice types visually by sea ice experts (Fig. 9 b): A is LFYI, where ridges cover less 20% of ice surface, B is first-year ice, where ridges cover more than 20% of ice surface, C is MYI area, and D is thick FYI and second-year ice. The ice types inside each zone were missed

(a)　　　　　　　　　　　　　　　　　(b)

of broken MYI. The SAR signature of such mixture of MYI and FYI can be generalized to be valid for larger areas.

An example of classification results is shown in Fig. 8 where the SAR image from January 18, 2008, covers the transition zone between MYI and FYI north of the Barents Sea. The image was divided into zones of four ice types: A is LFYI, where ridges cover less than 20% of ice surface; B is FYI, where ridges cover more than 40% of ice surface; C is MYI area; and D is ON [Fig. 8(b)]. The result of the NN classification is shown in Fig. 8(c) with the ice expert's analysis superimposed.

The confusion matrix between classification results and expert analysis gives 86%, 73%, 65%, and 38% correspondences in areas A, B, C, and D, respectively [Table IV(a)]. This is a relatively good result because the ice structure is very complex and the expert analysis does not take into account all the small features in the image. The result also shows difficulties in separating ON from LFYI, although some ON in leads could be classified in the MYI region (area C). The backscattering from open water, nilas, and LFYI can be similar, and in some cases, experts cannot distinguish them in SAR images without
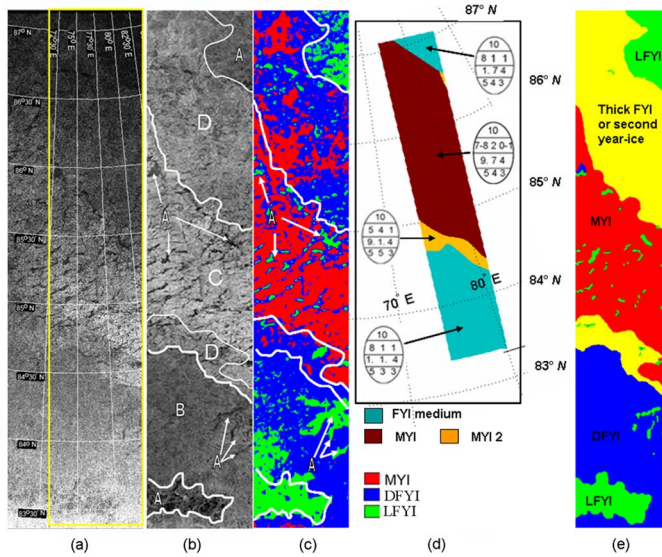
Fig. 9. (a) Fragment of original ENVISAT WS SAR image (HH polarization), taken over the northern part of the Kara Sea on February 04, 2008, at 11:00 UTC with geographical grid where near range is in the lower part and far range is in the upper part, where yellow box shows a classified part of the image. (b) Fragment of SAR image after normalization of $\sigma°$ to an incidence angle of 25° and analysis by an ice expert from AARI: A is LFYI, where ridges cover less than 20% of the ice surface; B is FYI, where ridges cover more than 40% of the ice surface; C is MYI area; and D is thick FYI and second-year ice. Arrows show the location of small ice features, marked by corresponding characters. (c) Result of NN classification. (d) Ice chart provided by AARI for February 06, 2008. The lower legend is for the SAR classification, and the upper legend is for the ice chart. (e) Manually colored image according to sea ice expert's visual analysis.
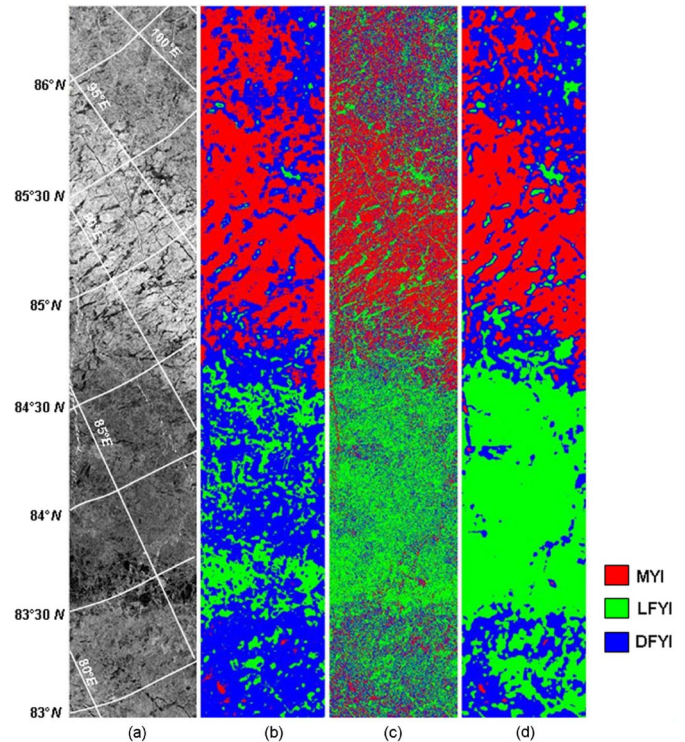

Fig. 10. Sea ice classification of original ENVISAT WS SAR image (HH polarization), taken over in the NP-35 area, north of the Barents Sea on January 14, 2008, at 11:59 UTC. (a) Fragment of SAR image with normalized $\sigma°$ to an incidence angle of 25°. (b) Result of NN classification for three sea ice types. (c) Bayesian-approach-classified image. (d) Bayesian-approach-classified image by averaging in a sliding window 32×32 and with moving step equaled four.

additional information. Therefore, our further analysis deals with the classification of three ice types—LFYI, DFYI, and MYI.

Another SAR image for February 4, 2008, covering the transition zone from FYI to MYI, was classified using three ice types [Fig. 9(a)]. The experts delineated areas marked as the following: LFYI, where ridges cover less than 20% of the ice surface (A); DFYI, where ridges cover more than 40% of the ice surface (B); MYI area (C); and thick FYI and second-year ice (D). The NN classification gave 72% correspondence with expert analysis in area C with predominant MYI. In areas A and B+D, correspondences between NN classification and expert analysis were 62% and 73%, respectively [Table IV(b)]. Some areas of MYI, LFYI, and DFYI were erroneously classified, particularly in small patches embedded in larger areas of homogeneous ice. The expert analysis suggested that second-year ice or smaller forms of MYI are present in area D. The NN was not trained to classify this ice type and will therefore tend to classify these areas as MYI or DFYI. In summary, this example shows that MYI floes and areas of LFYI were, to a large extent, classified correctly, while classification of DFYI is more difficult. This can be explained by the fact that the DFYI characteristics used in the classification tend to be located between MYI and LFYI, both in backscatter [Fig. 1(b)] and in some of the textural characteristics [Fig. 6(a) and (c)].

The results of NN classification were also compared with digital ice chart for January 16–18 [Fig. 8(d)], 2008, and February 6 [Fig. 9(d)] for the Kara Sea, where only one FYI class is used [Fig. 9(d)]. This implies that LFYI and DFYI from

the NN classification cannot be validated separately but jointly as one class. This joint class corresponds to FYI shown in ice charts by 93% and 99%, respectively. The MYI result shows correspondences of about 64% and 46%, respectively. However, the MYI area is not very accurately estimated in the ice charts because information comes mainly from visible and IR satellite images.

The best method available in this study is the expert analysis, because the expert has spent time to analyze the SAR images in more detail. The method was used to validate the 20 classified SAR images (see Fig. 7 and Table I). The average correspondences in NN and expert classifications, calculated from this series of ASAR images, acquired both from ascending and descending orbits, amount to 85%, 83%, and 80% for LFYI, DFYI, and MYI, respectively. The NN consistently distinguishes MYI areas from those with predominant FYI. Within MYI massifs, it identifies wide leads, although ice type in leads could be misclassified in some cases.

B. Results from the Bayesian Classification

Twelve ENVISAT ASAR images, acquired in the Central Arctic, were also classified using a Bayesian algorithm in order to compare classification results from two different methods (Table I). The preprocessing of the SAR images is similar to the NN method and consists of calibration, normalization to incidence angle of 25°, and also speckle reduction using

TABLE V
Confusion Matrix for Comparison of the Following: (a) Bayesian Classification Results Versus AARI Ice Charts; (b) Two Classification Methods, Applied to ENVISAT ASAR Images: January 14, 2008 [Comparison of Fig. 10(b) with Fig. 10(b)], January 18, 2008 (see Fig. 8), and February 4, 2008 (see Fig. 9). SAR Images Were Averaged Using $window\ size = 32 \times 32$ and $sliding\ step = 4$ Pixels Before Bayesian classification

AARI ice chart (as predicted)						
Assigned pixels classes (Bayesian)	%	14.01.2008		18.01.2008		04.02.2008
		FYI	MYI	FYI	MYI	FYI MYI
	FYI+DFYI	94.27	5.7	93.68	6.3	99.27 0.72
	MYI	39.2	60.2	49.28	50.7	50.2 49.76

(a)

AARI ice chart (as predicted)						
Assigned pixels classes (Bayesian)	%	14.01.2008		18.01.2008		04.02.2008
		FYI	MYI	FYI	MYI	FYI MYI
	FYI	59.3	7.5	67.8	12.6	65.93 11.81
	DFYI	34.9	32.3	26.7	35.9	33.35 38.41
	MYI	5.7	60.2	6.2	51.5	0.72 49.76

(b)

averaging by a 4×4 pixel sliding window. An example of classification by the two algorithms is shown in Fig. 10. The Bayesian algorithm was applied twice to this image, acquired on January 14, 2008, at 11:59 UTC [Fig. 10(a)], first, with a 4 $\times$ 4 pixel resolution [Fig. 10(c)] and, then, with averaged 32 $\times$ 32 pixels to present a classified image with the same resolution as the NN algorithm [Fig. 10(d)]. The classification results look quite similar [Fig. 10(b)–(d)], and higher resolution provides a more detailed classification, allowing better detection of leads and other small-scale features. On the other hand, the higher resolution also implies more noise in the classification results. The lower resolution shows results that are comparable to the NN results.

The main result is that MYI and FYI were generally identified correctly by both methods. The major difference is that the Bayesian method shows a larger area of LFYI, whereas the NN method shows a predominance of DFYI. There are no validation data to provide evidence which ice type is predominant. Both methods show wide leads in MYI, but the Bayesian method seems to classify ice in the leads as LFYI, which is more correct than DFYI from the NN method. This misclassification may be caused by using sliding window for textural characteristic calculation in the NN algorithm. The size of this sliding window is comparable with the typical size of small-scale ice features. In the case of Bayesian classification, lower values of $\sigma°$ for LFYI and higher values for MYI tend to be averaged within the sliding window, and the resulting value appear as DFYI. Bright narrow features in the area of FYI are leads with frost flowers. They were mostly classified as MYI, because the Bayesian algorithm does not include young ice, since its backscatter is similar to that of MYI [Fig. 1(b)].

Confusion matrices have been calculated to compare the classification results of the NN and Bayesian algorithms, applied to 12 SAR images, with ice charts (Table III). SAR images were averaged in a sliding window of 32×32. The comparison was made for MYI and FYI zones, delineated in the digital AARI ice charts. The total classification accuracies (diagonal elements of confusion matrix) were 68.1% for MYI and 95.7%

for FYI. Comparisons of Bayesian classification results for images shown in Figs. 8(a), 9(a), and 10(a) with ice charts are presented in Table V(a). The total classification accuracies were 50.7%, 49.8%, and 60.2% for MYI and 93.7%, 99.3%, and 94.3% for FYI. Therefore, FYI was classified quite well. Correspondence for MYI is not so good, probably due to limitations in using SAR data for ice chart composition. Comparison of Bayesian classification results for images shown in Figs. 8(a) and 9(a) with visual expert analysis [Figs. 8(e) and 9(e)] is presented in Table IV. In this case, the total classification accuracies were 52.4% and 67.9% for MYI, 73.1% and 94.4% for LFYI, and 24.9% and 55.9% for DFYI. Poor accuracy in DFYI classification may be explained by subjectivity in distinguishing LFYI from DFYI in the process of SAR image visual interpretation.

The confusion matrix in Table V(b) shows the correspondence of NN and Bayesian SAR sea ice classification results. In our case, when both data sets are not perfect, it is possible to estimate the difference between the two data sets and not the error. Therefore, we estimate the similarity of the NN and Bayesian classification results by determining the relative number of equivalently classified pixels, belonging to each ice type. The correspondences of these two algorithms are from 97.8% to 99.1% for FYI, from 48.7% to 73.9% for DFYI, and from 47.1% to 87.8% for MYI.

VI. DISCUSSION AND CONCLUSION

Algorithms of automatic NN-based and Bayesian classifications of sea ice types from ENVISAT ASAR images have been created and tested for winter conditions in the high Arctic. The implementation of the algorithms requires normalization of the observed sea ice radar backscatter to a predefined incidence angle to compensate for its angular dependence. The backscatter normalization across the swath has been carried out for a reference incidence angle of $25°$ using linear functions of the radar backscatter angular dependence derived separately for the predominant ice types. The ice types selected for classification were multiyear, deformed first-year, level first-year, and ON. A fifth ice type, young ice, has been also analyzed for backscatter normalization but has not been used in the subsequent analysis. The reason was that this ice type was very scarce in the analyzed images, implying that it was difficult to find enough data for training of the NN method. The remaining four ice types have different but partly overlapping radar backscatter value ranges in SAR images. Therefore, algorithms using only backscatter data will give ambiguous classification in many cases. By the use of various texture features of the ice types in addition to backscatter data, the hypothesis has been that ice classification should be improved.

Before the NN algorithm was applied, several image texture features together with backscatter values have been investigated for each ice type, using a training data set. The correlation coefficients between pairs of texture features have been calculated for each ice type, showing that correlation, inertia, cluster prominence, energy, homogeneity, and entropy, as well as third and fourth central statistical moments of image brightness,

could be used for the identification of these ice types. Different sizes of the sliding window for texture calculation have been tested, and the result has been that a window size of 32×32 pixels and a co-occurrence distance (distance between pixels) of four gave the best separation between the four ice types. Furthermore, several NN topologies with various numbers of hidden layers and neurons in these layers have been tested by the classification of 12 SAR images. Based on analysis of classification errors and processing time, it has been found that the optimal topology of the NN consisted of nine neurons in input layer, six neurons in hidden layer, and three neurons in output layer. The selected topology was then used in the NN to run classification algorithm on the training data. The ice classes used for training have been reproduced with high accuracy, showing that the algorithm was self-consistent. The algorithm was then ready for use to classify a new SAR data set. The classification results of these images have been also compared with ice charts issued by AARI, where MYI and FYI have been discriminated. The total classification accuracies, determined by the confusion matrix between classification results and ice charts, have been 79.3% for MYI and 92.5% for FYI.

A series of 20 ENVISAT ASAR images of sea ice has been classified using the NN algorithm described in Sections III–V. The images have been selected as representative for winter sea ice in the Central Arctic. Comparison of classification results with expert analysis has shown that the NN algorithm can distinguish MYI from areas with predominant LFYI, DFYI, and ON. Within the MYI massif, it can also identify relatively wide leads, whereas classification between open water, nilas, and other thin ice types has not been attempted. To simplify the classification, open water and nilas were treated as one ice type, characterized by lower backscatter than the other ice types. Classification results have been compared with visual analysis of the images by experts, who analyzed the SAR images in more detail. The ice experts have estimated the partial concentration for each ice type. This partial concentration was then compared with the partial percentage of each ice class from the NN analysis. The average correspondences in the NN classification of ASAR image series, as compared with visual expert's estimates, amount to 85%, 83%, and 80% for LFYI, DFYI, and MYI, respectively.

The Bayesian classification algorithm has used *a priori* probabilities of LFYI, DFYI, and MYI appearance in the Central Arctic. These probabilities have been estimated from knowledge of ice conditions, and conditional probabilities of these ice types have been derived from calibrated ENVISAT ASAR WS images. The Bayesian algorithm uses only backscatter but correctly classifies major sea ice types due to big differences in their *a priori* probabilities, as well as leads in sea ice. Correspondences of the Bayesian ice classification results for SAR images and ice charts for the same periods amount to 68.1% for MYI and 95.6% for FYI.

A comparison of confusion matrices shows a correspondence of Bayesian and NN classification results for LFYI and MYI in the Central Arctic. The NN classification results are less noisy, whereas pixel-by-pixel Bayesian algorithm better detects narrow leads in ice cover. NN allows detecting wide leads, which are important for climate studies and ice navigation.

The possibility to detect leads, as well as other small-scale ice features, is limited by the size of sliding window, used for textural characteristic calculation. When using 32×32 size and pixel spacing of 75 m, the minimum size of ice features is limited to 1200 m.

The Bayesian and NN algorithms may be effectively used in the Central Arctic where MYI is predominant. However, they hardly can be used in the marginal ice zone, where there is a mixture of many different ice types and their SAR signatures significantly depend on the size of ice floes. Classification accuracy can be improved by using SAR images at different polarizations, and the next step of this study is the development of sea ice classification from multipolarization data, as well as from SAR images in other spectral bands. The automatic SAR ice classification can be implemented as part of the GMES services for operational sea ice monitoring using data from RADARSAT-2, Sentinel-1, and other SAR satellites.

REFERENCES

[1] C. Tsatsoulis and R. Kwok, *Analysis of SAR Data of the Polar Oceans: Recent Advances.* Berlin, Germany: Springer-Verlag, 1998.

[2] S. Sandven, O. M. Johannessen, M. W. Miles, L. H. Pettersson, and K. Kloster, "Barents Sea seasonal ice zone features and processes from ERS-1 synthetic aperture radar: Seasonal ice zone experiment 1992," *J. Geophys. Res.*, vol. 104, no. C7, pp. 15 843–15 857, Jul. 1999.

[3] S. Sandven, O. Dalen, M. Lundhaug, K. Kloster, V. Y. Alexandrov, and L. V. Zaitsev, "Sea ice investigations in the Laptev Sea area in late summer using SAR data," *Can. J. Remote Sens.*, vol. 27, no. 5, pp. 502–516, 2001.

[4] V. Y. Alexandrov, S. Sandven, K. Kloster, L. P. Bobylev, and L. V. Zaitsev, "Comparison of sea ice signatures in OKEAN and RADARSAT radar images for the northeastern Barents Sea," *Can. J. Remote Sens.*, vol. 30, no. 6, pp. 882–892, 2004.

[5] O. M. Johannessen, V. Alexandrov, I. Frolov, L. Bobylev, S. Sandven, M. Miles, L. Pettersson, K. Kloster, V. Smirnov, Y. Mironov, and N. Babich, *Remote Sensing of Sea Ice in the Northern Sea Route: Studies and Applications.* Chichester, U.K.: Springer-Praxis, 2007.

[6] J. Haarpaintner and G. Spreen, "Use of enhanced-resolution QuikSCAT/SeaWinds data for operational ice services and climate research: Sea ice edge, type, concentration, and drift," *IEEE Trans. Geosci. Remote Sens.*, vol. 45, no. 10, pp. 3131–3137, Oct. 2007.

[7] W. Dierking and J. Dall, "Sea-ice deformation state from synthetic aperture radar imagery—Part I: Comparison of C- and L-band and different polarization," *IEEE Trans. Geosci. Remote Sens.*, vol. 45, no. 11, pp. 3610–3622, Nov. 2007.

[8] "World Meteorological Organization," WMO Sea Ice Nomenclature, Geneva, WMO Rep. 259, 1989.

[9] O. M. Johannnessen, A. Volkov, V. Grischenko, L. Bobylev, V. Asmus, T. Hamre, K. Kloster, V. Melentyev, S. Sandven, V. Smirnov, J. Solhaug, and L. Zaitsev, "ICEWACH: Ice SAR monitoring of the Northern Sea Route," in *Proc. 1st Int. Conf. EuroGOOS, 7-10 Oct. 1996—Operational Oceanography: The Challenge for European Cooperation*, J. H. Stell, H. W. A. Behrens, J. C. Borst, and L. J. Droppert, Eds., 1997, vol. 62, pp. 224–233.

[10] R. D. Abreu, "RADAR sea ice signatures: An operational primer," in *Proc. Workshop Mapping Archiving Sea Ice Data—The Expanding Role Radar*, Ottawa, ON, Canada, May 2–4, 2000, pp. 85–94, JCOMM Tech. Rep. no. 7, 2000.

[11] W. Dierking, "Mapping of different sea ice regimes using images from Sentinel-1 and ALOS synthetic aperture radar," *IEEE Trans. Geosci. Remote Sens.*, vol. 48, no. 3, pp. 1045–1058, Mar. 2010.

[12] D. A. Clausi, "Texture analysis of SAR ICE imagery using MRFs," in *Proc. Workshop Mapping Archiving Sea Ice Data—The Expanding Role Radar*, Ottawa, ON, Canada, May 2–4, 2000, pp. 287–292, JCOMM Tech. Rep. no. 7, 2000.

[13] Q. Y. Yu and D. A. Clausi, "SAR sea-ice image analysis based on iterative region growing using semantics," *IEEE Trans. Geosci. Remote Sens.*, vol. 45, no. 12, pp. 3919–3931, Dec. 2007.

[14] Y. Hara, R. G. Atkins, R. T. Shin, J. A. Kong, S. H. Yueh, and R. Kwok, "Application of neural networks for sea ice classification in polarimetric SAR images," *IEEE Trans. Geosci. Remote Sens.*, vol. 33, no. 3, pp. 740–748, May 1995.

[15] R. Kwok, J. C. Curlander, R. McConnell, and S. S. Pang, "An ice-motion tracking system at the Alaska SAR Facility," *IEEE J. Ocean. Eng.*, vol. 15, no. 1, pp. 44–54, Jan. 1990.

[16] R. Kwok, G. F. Cunningham, and B. Holt, "An approach to identification of sea ice types from spaceborne SAR data," in *Microwave Remote Sensing of Sea Ice*, F. D. Carsey, Ed. Washington, DC: Amer. Geophys. Union, 1992, pp. 355–360.

[17] F. M. Fetterer, D. Gineris, and R. Kwok, "Sea ice type maps from Alaska Synthetic Aperture Radar Facility imagery: An assessment," *J. Geophys. Res.*, vol. 99, no. C11, pp. 22 443–22 458, Nov. 1994.

[18] L. K. Soh, C. Tsatsoulis, D. Gineris, and C. Bertoia, "ARKTOS: An intelligent system for SAR sea ice image classification," *IEEE Trans. Geosci. Remote Sens.*, vol. 42, no. 1, pp. 229–248, Jan. 2004.

[19] P. D. Heerman and N. Khazenie, "Classification of multispectral remote sensing data using a back-propagation neural network," *IEEE Trans. Geosci. Remote Sens.*, vol. 30, no. 1, pp. 81–88, Jan. 1992.

[20] C. Mejia, S. Thiria, N. Tran, M. Crépon, and F. Badran, "Determination of the geophysical model function of the ERS-1 scatterometer by the use of neural networks," *J. Geophys. Res.*, vol. 103, no. C6, pp. 12 853–12 868, Jun. 1998.

[21] D. Cornford, I. T. Nabney, and G. Ramage, "Improved neural network scatterometer forward models," *J. Geophys. Res.*, vol. 106, no. C10, pp. 22 331–22 338, Oct. 2001.

[22] J. A. Karvonen, "Baltic Sea ice SAR segmentation and classification using modified pulse-coupled neural networks," *IEEE Trans. Geosci. Remote Sens.*, vol. 42, no. 7, pp. 1566–1574, Jul. 2004.

[23] A. Bogdanov, S. Sandven, O. M. Johannessen, V. Alexandrov, and L. Bobylev, "Multisensor approach to automated classification of sea ice," *IEEE Trans. Geosci. Remote Sens.*, vol. 43, no. 7, pp. 1648–1664, Jul. 2005.

[24] C. C. Wackerman and D. L. Miller, "An automated algorithm for sea ice classification in the marginal ice zone using ERS-1 synthetic aperture radar imagery," ERIM, Ann Arbor, MI, Tech. Rep., 1996.

[25] ASAR User Guide. [Online]. Available: http://envisat.esa.int/handbooks/asar/CNTR2-11-5.htm

[26] F. T. Ulaby, R. K. Moore, and A. K. Fung, *Microwave Remote Sensing: Active and Passive*. Reading, MA: Addison-Wesley, 1981.

[27] J. Askne, A. Carlstrom, W. Dierking, and L. Ulander, "ERS-1 SAR backscatter modeling and interpretation of sea ice signatures," in *Proc. IGARSS*, Pasadena, CA, Aug. 8–12, 1994, pp. 162–164.

[28] R. Kwok, S. V. Nghiem, S. Martin, D. P. Winebrenner, A. J. Gow, D. K. Perovich, C. T. Swift, D. G. Barber, K. M. Golden, and E. J. Knapp, "Laboratory measurements of sea ice: Connections to microwave remote sensing," *IEEE Trans. Geosci. Remote Sens.*, vol. 36, no. 5, pp. 1716–1730, Sep. 1998.

[29] S. G. Beaven, S. P. Gogineni, and M. Shanablen, "Radar backscatter signatures of thin ice in the central arctic," *Int. J. Remote Sens.*, vol. 15, no. 5, pp. 1149–1154, Mar. 1994.

[30] D. Isleifson, B. Hwang, D. G. Barber, R. K. Scharien, and L. Shafai, "C-band polarimetric backscattering signatures of newly formed sea ice during fall freeze-up," *IEEE Trans. Geosci. Remote Sens.*, vol. 48, no. 8, pp. 3256–3267, Aug. 2010.

[31] V. Y. Alexandrov and N. Y. Piotrovskaya, "Assessment of the backscatter for various sea ice types from ENVISAT ASAR images," *Stud. Earth Space*, no. 4, pp. 3–11, Jul./Aug. 2008.

[32] V. Y. Alexandrov and N. Y. Piotrovskaya, "Digital processing of EN-VISAT ASAR images of the sea ice," *Problems Arctic Antarctic*, vol. 1, no. 78, pp. 90–94, 2008.

[33] H. Melling, "Detection of features in first-year pack ice by synthetic aperture radar (SAR)," *Int. J. Remote Sens.*, vol. 19, no. 6, pp. 1223–1249, Sep. 1998.

[34] K. C. Partington, J. D. Flach, D. Barber, D. Isleifson, P. J. Meadows, and P. Verlaan, "Dual-polarization C-band radar observations of sea ice in the Amundsen Gulf," *IEEE Trans. Geosci. Remote Sens.*, vol. 48, no. 6, pp. 2685–2691, Jun. 2010.

[35] R. Kwok and G. F. Cunningham, "Backscatter characteristics of the winter ice cover in the Beaufort Sea," *J. Geophys. Res.*, vol. 99, no. C4, pp. 7787–7802, Apr. 1994.

[36] R. G. Onstott, "SAR and scatterometer signatures of sea ice," in *Microwave Remote Sensing of Sea Ice*, F. D. Carsey, Ed. Washington, DC: Amer. Geophys. Union, 1992, pp. 73–102.

[37] R. Duda and P. Hart, *Pattern Classification and Scene Analysis*. New York: Willey, 1973.

[38] A. Benediktsson, P. H. Swain, and K. Ersoy Okan, "Neural network approaches versus statistical methods in classification of multisource remote sensing data," *IEEE Trans. Geosci. Remote Sens.*, vol. 28, no. 4, pp. 540–552, Jul. 1990.

[39] S. Haykin, *Neural Networks: A Comprehensive Foundation*, 2nd ed. Englewood Cliffs, NJ: Prentice-Hall, 1999.

[40] Y. Hara, R. G. Atkins, R. T. Shin, J. A. Kong, S. H. Yueh, and R. Kwok, "Application of neural networks to radar image classification," *IEEE Trans. Geosci. Remote Sens.*, vol. 32, no. 1, pp. 100–109, Jan. 1994.

[41] R. M. Haralick, K. Shanmugan, and I. Dinstein, "Textural features for image classification," *IEEE Trans. Syst. Man, Cybern.*, vol. SMC-3, no. 6, pp. 610–621, Nov. 1973.

[42] L. K. Soh and C. Tsatsoulis, "Texture analysis of SAR sea ice imagery using gray level co-occurrence matrices," *IEEE Trans. Geosci. Remote Sens.*, vol. 37, no. 2, pp. 780–795, Mar. 1999.

[43] D. A. Clausi, "An analysis of co-occurrence texture statistics as a function of grey level quantization," *Can. J. Remote Sens.*, vol. 28, no. 1, pp. 45–62, 2002.

[44] M. E. Shokr, "Evaluation of second-order texture parameters for sea ice classification from radar images," *J. Geophys. Res.*, vol. 96, no. C6, pp. 10 625–10 640, Nov. 1990.

[45] W. Pratt, *Digital Image Processing: Translation from English*. Moscow, Russia: MIR, 1982.

[46] A. Baraldi and F. Parmiggiani, "An investigation of the textural characteristics associated with gray level cooccurrence matrix statistical parameters," *IEEE Trans. Geosci. Remote Sens.*, vol. 33, no. 2, pp. 293–304, Mar. 1995.

Natalia Yu. Zakhvatkina received the B.S. degree from the Russian State Hydrometeorological University, Saint Petersburg, Russia, in 2003 and the Ph.D. degree in oceanology from the Arctic and Antarctic Research Institute (AARI), Saint Petersburg, in 2009, in cooperation with the Nansen International Environmental and Remote Sensing Centre (NIERSC), Saint Petersburg.

Since 2009, she has been a Scientist with AARI, where she was an Engineer in the department of ice information system development, and with NIERSC, where she worked on the remote sensing of sea ice, satellite sea ice data assimilation and interpretation, automatic classification of sea ice, and neural network technique.

Vitaly Yu. Alexandrov received the Ph.D. degree in oceanology from the Arctic and Antarctic Research Institute (AARI), Saint Petersburg, Russia, in 1981. In 2010, he defended Doctor of Science thesis in oceanology at AARI.

From 1983, he was a Senior Scientist with AARI, where he worked on sea ice remote sensing and development of the automated algorithms of image interpretation. Since 1997, he has been with the Nansen International Environmental and Remote Sensing Centre, Saint Petersburg, where he works as a Senior Scientist on the synthetic aperture radar (SAR) remote sensing of sea ice. He is a leader of several national and international research and application projects with focus on sea ice and participated in several Arctic expeditions. Since 2010, he has also been with the Nansen Environmental and Remote Sensing Center, Bergen, Norway. He has published about 20 papers in international refereed journals and books. His research interests include the demonstration of SAR data use onboard the icebreakers in the Northern Sea Route, interpretation of sea ice types and features in SAR images, *in situ* measurements of sea ice and snow properties, and climatic changes in the Arctic.

Ola M. Johannessen received the Cand. Real. degree in physical oceanography from the Geophysical Institute, University of Bergen (UoB), Bergen, Norway, in 1965.

He has held different faculty and research positions with the University of Sao Paulo, Sao Paulo, Brazil, and the North Atlantic Treaty Organization Research Center, Italy, before returning to UoB in 1974, where he is a Professor Emeritus. He is currently a Nansen Fellow and the Founding Director Emeritus of the Nansen Environmental and Remote Sensing Center (NERSC), Bergen. He is currently involved in the following scientific fields: Arctic climate system, including sea ice and Greenland ice sheet variability; climate teleconnection between low and high latitudes and vice versa; operational oceanography; Indian Bay of Bengal and Southern Ocean circulation and sea level studies; and socioeconomic impact studies of global change. He is the author and coauthor of more than 500 publications of which eight are books and 148 are in refereed journals, books, and proceedings. He is also currently a Member of the editorial board of PRAXIS Publishing Ltd. and Co-Chief Editor of the journal *Atmospheric and Oceanic Science Letter* of the Chinese Academy of Science (CAS), Beijing, China.

Prof. Johannessen is an elected full member of the International Academy of Astronautics, the European Academy of Science and Arts, the Finnish Academy of Science and Letters, the Norwegian Academy of Technical Sciences, the Norwegian Academy of Science and Letters, and the Norwegian Scientific Academy for Polar Research. He is the President of the Nansen Scientific Society; the President of the Norwegian Scientific Academy for Polar Research; the Chairman of the Guardian Board of the Nansen International Environmental and Remote Sensing Centre (NIERSC), Saint Petersburg, Russia; the Chairman of the Board of the Nansen Center, Cochin, India; the Cochairman of the Board of the Nansen-Zhu International Research Center, Institute of Atmospheric Physics, CAS; Cochairman of the Board of the Nansen-Tutu Marin Center, University of Cape Town, Cape Town, South Africa; and Leader of the Nansen Group. He is also currently a Council Member of the European Climate Forum. Furthermore, he is a member of the Scientific Advisory Committee of the Euromediterranean Center for Climate Change, Italy. He was the Laureate of the European Union Descartes Prize in Earth Science in 2005 for leading the project Climate and Environmental Change in the Arctic. He was a recipient of the Fridtjof Nansen Medal for Outstanding Research in 2007 by the Norwegian Academy of Science and Letters. In 2008, His Majesty King Harald V of Norway appointed him to the Royal Norwegian Saint Olav decoration, Knight of First Class. In 2010, he was awarded the honorary membership from the Norwegian Academy of Technological Sciences (NTVA) and received the "Certificate" from the Director General of the European Space Agency for his contribution to the "High-Level Science Policy Advisory Committee from 2007 to 2010." In 2011, he was a recipient of "the Norwegian Space Center award for his scientific contribution to increase international awareness and understanding of space activities—in particular, for earth observations."

Stein Sandven received the Cand. Real. degree in physical oceanography from the Geophysical Institute, University of Bergen (UoB), Norway, in 1979. In 2006, he started Professor at the University Centre in Svalbard (UNIS). Employed as scientist at the Nansen Environmental and Remote Sensing Center (NERSC), Bergen, Norway, when it was started in 1986, he is currently a Director with the NERSC.

He is Director with the Nansen Environmental and Remote Sensing Center, Bergen, Norway. He is a leader of several national and international marine research and application projects, with a focus on remote sensing application and operational ice/ocean monitoring. His research activities are mainly in the areas of remote sensing of sea ice and oceanographic processes including ocean acoustics. In sea ice research, data from different types of satellite sensors are used for studies of sea ice classification, drift, thickness, and processes such as leads, polynyas, and ridges. Validation of sea ice remote sensing data uses data from *in situ* observations. The research is focused on the development of operational observing systems for the Arctic seas using satellite, *in situ*, and underwater sensors. He has presented the scientific work at many national and international conferences since 1986. He is a Coordinator of several European Union projects under environmental, climate, and IST programs. He has published about 60 papers in international refereed journals and books.

Ivan Ye. Frolov received the B.S. degree from the Leningrad Hydrometeorological Institute, Saint Petersburg, Russia, in 1971.

Since 1992, he has been the Director of the Arctic and Antarctic Research Institute, Saint Petersburg, Russia, where he was an Engineer with the Department of Ice Regime. He has 41 years of experience in the field of research and coordination of Russian national and international activities in the Arctic and Antarctic Regions in the position of Scientist, Head of laboratory. He is a Doctor of geographical sciences and, in 2005, was awarded the title Professor of oceanography with the Russian State Hydrometeorological University, Saint Petersburg. His research activities are mainly in the areas of sea ice, oceanology, and climate research. He directly participated in more than 30 Arctic and Antarctic expeditions, and in 20 of them, he was the Scientific or Operations Leader. Among these were a research expedition on board nuclear icebreaker (IB) "Sibir," which, in May 1987, reached the North Pole, and an Arctic voyage research vessel "Akademik Fedorov" when the North Pole was reached for the first time by a non-IB ship. He was the Operation Leader for launching ice drifting research stations "North Pole 33 and 34." He was a Coordinator and Scientific Advisor of two subprograms for polar regions of national research program "World Ocean."

Prof. Frolov was a Member of the Russian National Committee on International Polar Year 2007–2008 and National Oceanographic Committee. He has been the Cochair of the World Meteorological Organization (WMO) Global Digital Sea Ice Data Bank since 1989, was the Chairman of the former WMO Commission for Marine Meteorology Subgroup on Sea Ice in 1989–2001, has been a Member of the Joint Technical Commission for Oceanography and Marine Meteorology Management Committee since 2001, and is the Cochair of the Committee in the Framework of Agreement on Science and Technology Cooperation in Arctic and North Research between the Ministry of Science and Technologies of the Russian Federation and the Research Council of Norway. He was a recipient of high governmental and ministerial honors: Order of Labour Red Banner (1987), "Honorary Polar Explorer," "Honorary Worker of Marine Fleet," "Honorary Worker of Hydrometeorology Service of Russia," Russian Government prizeman in the field of science and techniques (2002), Order of Honor of Russia (2005), and "Honored Scientist of Russia" (2009).